Influence of fiber orientation on the mechanical responses of engineering cementitious composite (ECC) under various loading conditions

Tawfek, Abdullah M. ; Ge, Zhi; Yuan, Huaqiang ; Zhang, Ning ; Zhang, Hongzhi; Ling, Yifeng ; Guan, Yanhua ; Šavija, B.

Publication date
2023

Document Version
Final published version

Published in
Journal of Building Engineering

Citation (APA)
Tawfek, A. M., Ge, Z., Yuan, H., Zhang, N., Zhang, H., Ling, Y., Guan, Y., & Šavija, B. (2023). Influence of fiber orientation on the mechanical responses of engineering cementitious composite (ECC) under various loading conditions. *Journal of Building Engineering*, *63*(B).

Journal of Building Engineering 63 (2023) 105518

Contents lists available at ScienceDirect

Journal of Building Engineering

journal homepage: www.elsevier.com/locate/jobe

Influence of fiber orientation on the mechanical responses of engineering cementitious composite (ECC) under various loading conditions

Abdullah M. Tawfek [a,b], Zhi Ge [a], Huaqiang Yuan [a], Ning Zhang [c], Hongzhi Zhang [a,d,*], Yifeng Ling [a,**], Yanhua Guan [a], Branko Šavija [e]

[a] School of Qilu Transportation, Shandong University, 250002, Jinan, PR China
[b] Sana'a University, 12544, Sanaa, Yemen
[c] Shandong Hi-Speed Group, 266061, Jinan, PR China
[d] Suzhou Research Institute, Shandong University, 215021, Suzhou, PR China
[e] Microlab, Faculty of Civil Engineering and Geosciences, Delft University of Technology, 2628 CN, Delft, the Netherlands

ARTICLE INFO

Keywords:
Engineering cementitious composite
Fiber orientation
Mechanical behavior
Digital image correlation
Crack width

ABSTRACT

The mechanical performance of engineered cementitious composite (ECC) depends greatly on fiber orientation and distribution. In this paper, the effect of fiber orientation on ECC's mechanical properties was investigated using two different casting methods: a flow-induced casting was used to enhance the fiber orientation within ECC mixture and compared with the conventional casting. The fiber orientation was quantified using scanning electron microscope (SEM) and image processing. Mechanical tests on the specimens with various fiber orientations were performed. The failure processes of ECC specimens under compression and tensile tests were analyzed using digital image correlation (DIC) technique. The proposed flow-induced casting enhanced the fiber alignment in the flow direction. Consequently, ECC's mechanical properties were significantly improved with more finer cracks under uniaxial loading. In conclusion, the proposed flow-induced casting can be adopted as an effective approach to improve fiber bridging efficiency in ECC.

1. Introduction

Engineered cementitious composite (ECC) is a type of short fiber reinforced composite [1,2]. It exhibits pseudo-strain-hardening behavior and multiple cracking under tension [3]. The tensile strain capacity of ECC is in the range of 3%–8%, which is two orders of magnitude that of conventional concrete [4]. Moreover, the tensile strength of ECC is around 4–6 MPa, with compressive strength in the range of 30–80 MPa based on the mixture composition design [5]. Due to these characteristics, ECC has attracted a lot of attention.

The noticeable improvement of the mechanical and physical properties of ECC is mainly attributed to the lower w/b ratio [6] and fiber addition to the matrix [7]. The inclusion of the fiber enhances the tensile strength, strain capacity, flexural strength, fracture toughness, durability, and fire resistance of the cementitious composite [8–10]. The introduction of fiber into the cementitious matrix has two major effects: first, they act as micro-reinforcement, prevent microcrack propagation and delay the onset of the tensile cracks.

* Corresponding author. School of Qilu Transportation, Shandong University, 250002, Jinan, PR China.
** Corresponding author.
E-mail addresses: hzzhang@sdu.edu.cn (H. Zhang), yfling@sdu.edu.cn (Y. Ling).

https://doi.org/10.1016/j.jobe.2022.105518
Received 9 September 2022; Received in revised form 3 November 2022; Accepted 6 November 2022
Available online 21 November 2022

Table 1
The mixture proportions of PVA-ECC (kg/m^3).

Cement	Fly ash	Sand	PVA fiber	Water	HRWRA	VMA	w/b*
568	682	455	26	325	6.25	0.57	0.26

w/b* water to binder ratio.

Table 2
Chemical compositions of fly ash and cement (wt. %).

Oxides	Cement	Fly Ash
SiO_2	22.66	54.59
Al_2O_3	6.53	25.80
Fe_2O_3	3.05	6.96
CaO	58.26	5.49
SO_3	4.51	1.83
MgO	3.00	0.99
K_2O	0.76	1.76
TiO_2	0.55	1.26
MnO	0.33	0.11
P_2O_5	0.13	0.27
Specific gravity	3.15	2.32
Fineness %	2.22	2.86

Second, providing an interfacial transition zone ITZ (source of cracking sites) between cement mortar and the other particles within the matrix [11]. The micro-crack propagation of the matrix can be controlled by fiber bridging and fiber/matrix debonding [12]. The crack-bridging behavior of the fiber in ECC strongly depends on the fiber distribution and orientation relative to the loading directions [13,14]. The crack-bridging stress increases as the fiber inclination angle to the load direction decrease [15].

In general, up to 2%vol fiber is used in ECC [16,17]. Several researchers studied the effect of fiber content on the mechanical properties of ECC. They concluded that the mechanical properties of ECC improve with an increase in fiber content due to the increase in fiber number in the unit cross-section, which enhances its ability to resist cracking. However, the excessive fiber content can result in agglomeration and non-uniform dispersion of the fibers. Thus, the mechanical properties and durability of ECC decrease due to the low workability of the mixture [18–21].

One of the main reasons for the variance in the flexural and tensile strength of the cementitious composite at the same fiber content is mostly due to the fiber effect, such as fiber properties (fiber type, fiber content, aspect ratio) [22–25], fiber/matrix interfacial bond [26], as well as fiber distribution and orientation [11,27,28]. The former two parameters can be adjusted during mixture design, while the fiber distribution and orientation can be controlled during production.

In general, the production cost of the ECC is higher than conventional concrete. This can be mainly attributed to the use of polymeric fiber [29,30]. This kind of fiber can be bent within the mixture during the casting, leading to fiber ball formation and non-uniform dispersion, resulting in a lack of homogeneity [8,31]. Therefore, decreasing the fiber content while maintaining the advantage of ECC is a major point of research. It can reduce the ECC production cost, simplify the flow and casting process, decrease fiber ball occurrence, and improve the microstructure of the ECC. This would open the way for more widespread practical applications [32]. Improving the fiber orientation and distribution has been considered as an effective way to achieve this.

Modifying fiber properties [33], mixing procedure [34], rheology, matrix flowability, casting process, wall effect [24,35–39], and specimen thickness [2] have been employed to enhance the fiber distribution and orientation in the cementitious composite, leading to improved mechanical properties. Among those, flow-induced approach can be considered the most effective [24,35], where the flow-induced cast approach tends to promote axial fiber orientation in the flow direction. For steel fibers, numerous studies have been carried out to investigate the effect of fiber orientation and casting method on concrete. Groth & Nemegeer [40] stated that the fiber orientation in freshly mixed concrete exhibits flow-dependent characteristics. Huang et al. [41] utilized the flow-induced casting method using L-shaped device to enhance the steel fiber orientation during UHPC placement. They concluded that this casting method could improve the fiber alignment in the flow direction, leading to 65% higher flexural strength than the conventional casting method.

The fiber distribution and orientation can be governed through a balanced set of carefully designed casting approach and the fresh state properties of the cementitious mixture. However, limited experimental studies have been conducted to assess the effect of the PVA fiber alignment on the cementitious composite. In the authors' previous work [42], the flow-induced approach has been successfully used to improve the PVA fiber alignment during the casting process. Due to the constraints of the developed instruction device, the study was limited to the influence of fiber orientation on the flexural behaviors. The results indicate that flexural strength and deformability can be enhanced.

The current research focuses on the influence of fiber distribution and orientation on ECC response under various loading conditions. For this purpose, a flow-induced method was proposed to cast the ECC mixture, which enhances the fiber alignment with the flow direction. SEM and image processing techniques were applied to measure the fiber distribution and alignment degree. Uniaxial compression, splitting, four-point bending, and uniaxial tension tests were carried out. Combined with digital image correlation technique, the influence of fiber distribution and alignment degree on the cracking process was characterized, and the mechanism

Table 3
The mechanical and physical properties of PVA fibers.

Length (mm)	Diameter (μm)	Elongation (%)	Density (g/cm^3)	Tensile Modulus (GPa)	Tensile Strength (MPa)
12	40	7.0	1.3	39.5	1650

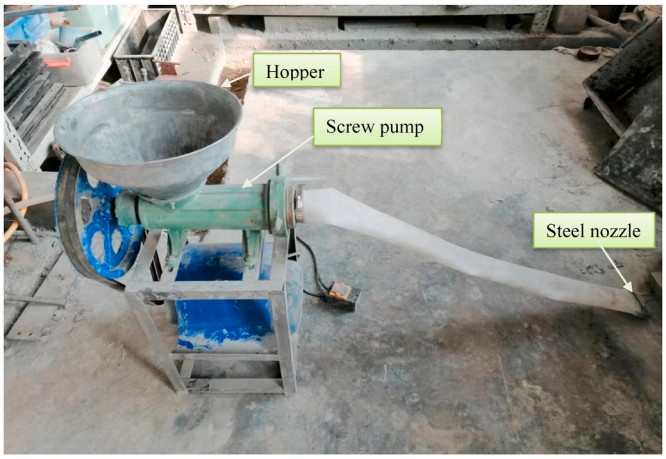

Fig. 1. The extrusion device with steel nozzle.

behind it was explained.

2. Experimental program

2.1. Materials and mixture proportions

Table 1 summarizes the ECC mixture proportions, which consists of ordinary Portland cement (OPC) with strength grade of 42.5 N, class F fly ash, Quartz sand, water, viscosity modifying agent (VMA), high range water reducing admixture (HRWRA), and PVA fiber. The water-to-binder ratio (w/b) was 0.26. Table 2 presents the chemical compositions of the fly ash and cement. Quartz sand has a grain size ranging from 80 to 120 μm and a median particle size of 100 μm. Hydroxypropyl methylcellulose (HPMC) VMA with a viscosity of 150,000 Pa s was chosen. Polycarboxylate ether (PCE)-based HRWRA was used. Its water reducing efficiency was about 20%. PVA fibers were used in this study. It was supplied by the Kuraray Corporation company-Japan. The mechanical and physical properties of PVA fibers are presented in Table 3.

2.2. Mixing process

All ECC mixtures were made following the same mixing protocol. For each mix, a 60-L capacity was used. About 20L material was produced for one batch. Cement, fly ash, silica sand, and VMA were first mixed without water for 2 min. Afterwards, the water mixed with HRWRA was added gradually for another 5 min mixing. Once a consistent and uniform mixture was reached, the fiber was gradually added. This was followed by 5 min of mixing. The fresh mixtures were then used for casting.

2.3. Casting process and specimen preparation

Two casting approaches (i.e., the flow-induced method and conventional method) were used to prepare specimens in the present study. For each casting method, three types of specimens were prepared, as shown in Fig. 2. They are: slabs with the dimension of 400 mm × 400 mm × 15 mm and prisms in size of 400 mm × 100 mm × 100 mm, and dog-bone specimen, whose dimensions are shown in Fig. 3. The same batch of fresh ECC mixture was used for both casting approaches.

In the conventional method, the mixture was manually poured into the molds. Specimens cast in this approach are termed as R-ECC, where the fiber is randomly distributed. Regarding the flow-induced method, an extrusion machine was used to enhance the fiber alignment with the flow direction. Specimens cast by this method are referred O-ECC, where the fiber is oriented with the flow direction. The machine mainly involves three modules, namely feeding, extrusion, and flow-induction (see Fig. 1). The feeding module consists of a hopper to pour the mixture through. The hopper was mounted to the screw pump (extrusion system) to discharge the fresh ECC mixture. The tube was connected to the extrusion module for the flow induction. Two sizes of the tube were used. The first tube consists of different diameters connected by an expander to increase the tube diameter. A steel nozzle was used to control the tube outlet with 300 mm × 10 mm dimension to cast the slab molds. Each slab consisted of two layers approximately 10 mm thick, and the extruded filament width was equal to the nozzle width in all layers. The casting direction was as illustrated in Fig. 2a.

The other tube has a diameter of 100 mm. It was used to cast the prismatic specimens with the size of 400 mm × 100 mm × 100 mm. In order to align the fibers with the flow direction during the extrusion phase, the outlet of the extruder tube was connected with a steel

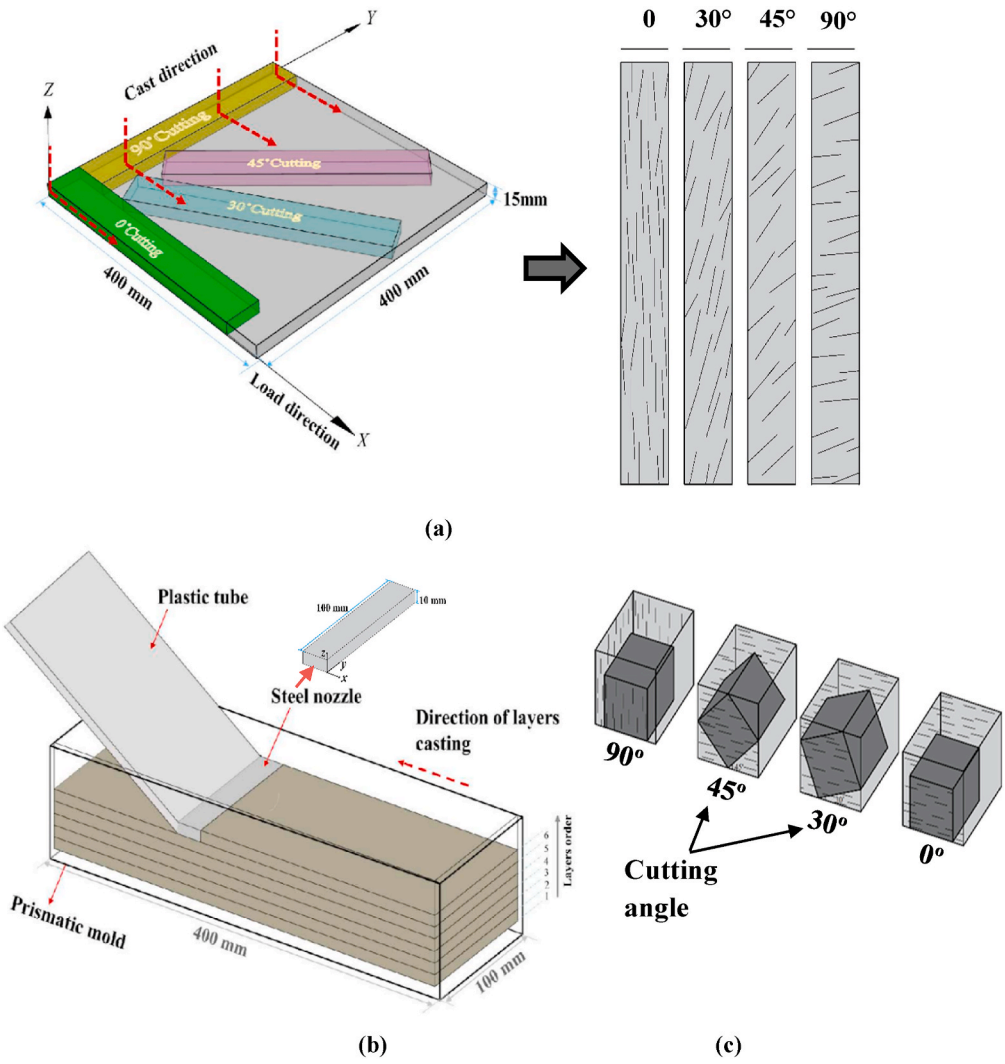

Fig. 2. Schematic description of casting and cutting directions of ECC specimens a) Slab specimen b) Prismatic specimen c) Different cutting angle.

nozzle having a size of 100 × 10 mm. The outlet nozzle opening in a z-direction (i.e. vertical direction) is 10 mm, as shown in Fig. 2b. It is less than the fiber length, limiting the fiber to rotate freely in the z-direction. Consequently, the fibers tend to align with the flow direction [37,43]. Ten layers were applied to cast each prismatic specimen layer by layer with approximately 10 mm layer height (see Fig. 2b). A slight external vibration (Formwork vibrator) was employed to eliminate the air bubbles. Two layers were cast using the same tube with the size of 100 × 10 mm for the dog-bone molds. The extrusion rate was 0.02 m/s for the prismatic specimen, 0.09 m/s for the dog-bone specimen, and 0.04 m/s for the slab specimen.

For the flexural test, five ECC slab specimens were cast, and four beam specimens measuring 350 × 50 × 15 mm were cut from each slab at the different cutting directions (0°, 30°, 45°, and 90° concerning the x-axis), see Fig. 2a. For compression and splitting testing, nine prismatic specimens for the compression and four prismatic specimens for the splitting were cast for both approaches. Then, three cubic specimens with the size of 70.7 × 70.7 × 70.7 mm were cut and prepared for each approach. Furthermore, three cubic specimens of 70.7 mm^3 were cut from O-ECC prismatic specimens (see Fig. 2c) at different fiber orientations (0°, 30°, 45°, and 90° concerning the x-axis). Finally, six dog-bone specimens were prepared for the tensile test. Note that the dog bone specimens were directly made by the two casting approaches, and only two cases (aligned and random fiber) were considered. Table 4 presents the load direction to fiber alignment of ECC specimens under different loading conditions. After casting, all specimens were levelled off and covered with the plastic film to avoid water evaporation, then de-molded after 24 h of the casting. Afterwards, the specimens were cured in the curing room at constant temperature (23 ± 3 °C) and relative humidity (98 ± 2) % until the testing date.

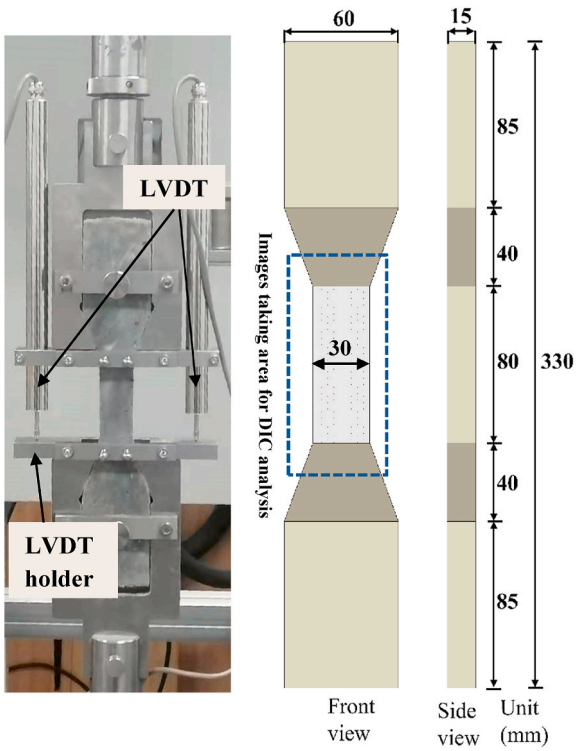

Fig. 3. Schematic description of tensile specimen and installation.

Table 4
The load direction to fiber alignment of ECC specimens under different loading conditions.

Sample name	Loading condition	Load direction to fiber alignment
C–O	Compression	oriented
CC-0		0°
CC-30		30°
CC-45		45°
CC-90		90°
C-R		random
S–O	Splitting	oriented
SC-0		0°
SC-30		30°
SC-45		45°
SC-90		90°
S-R		random
F–O	Flexural	oriented
FC-0		0°
FC-30		30°
FC-45		45°
FC-90		90°
F-R		random
T-0	Uniaxial tension	0°
T-90		90°
T-R		random

Note: C Compressive test, S splitting test, F Flexural test, T Tensile test, C-0, C-30, C-45, and C-90 Cutting direction relative to the load direction.

3. Test procedure

3.1. Uniaxial tension test

Uniaxial tension test was instrumented using an INSTRON 8801 machine. The test setup is shown in Fig. 3. Three dog-bone specimens were tested for each case. The test was under displacement control with a loading rate of 0.1 mm/min. Two linear variable displacement transducers (LVDT) were installed at the sides to measure the tensile deformation of the gauging zone (80 mm).

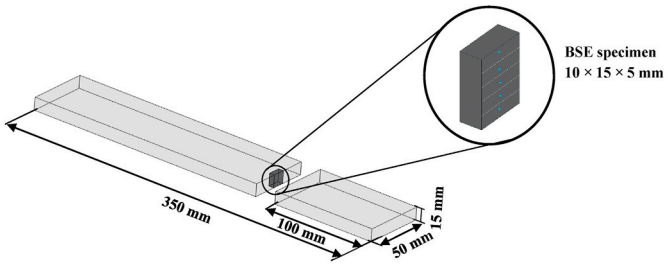

Fig. 4. BSE specimen cut from beam specimen after bending test.

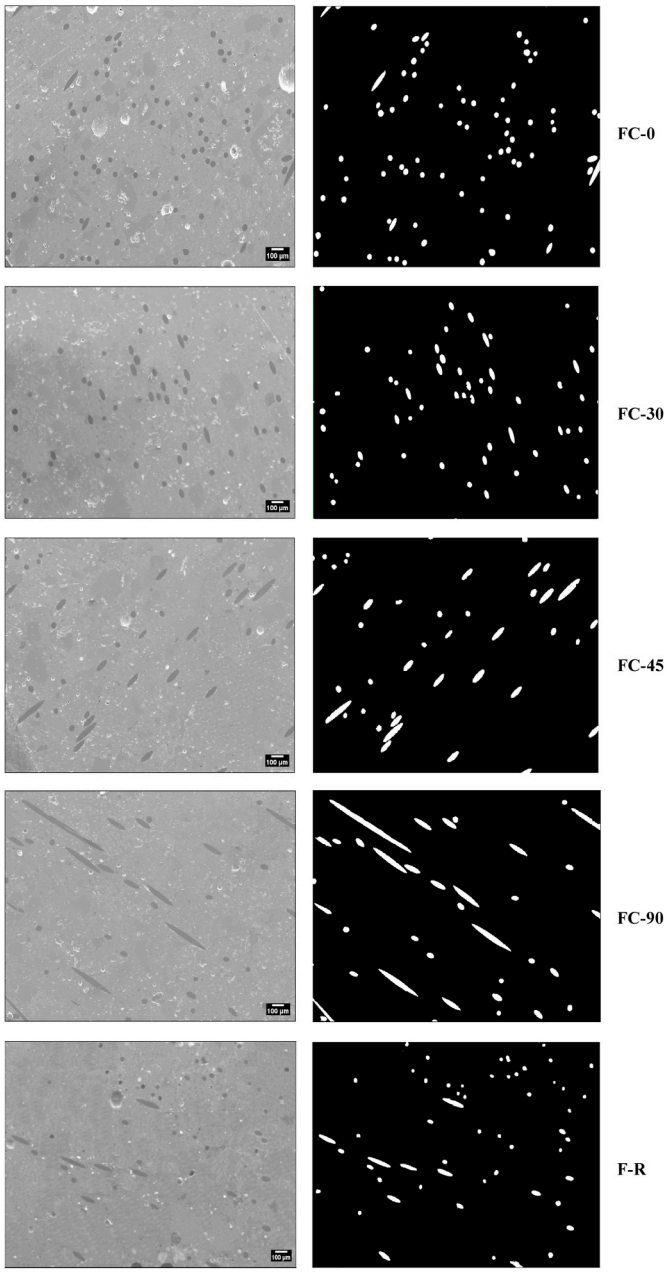

Fig. 5. Original microscope image and segmented fiber images at different cutting direction of the F–O and F-R slabs.

3.2. Uniaxial compression and splitting test

Uniaxial Compression and splitting tests were carried out using a universal testing machine (WDW-300). Before the test, a surface treatment was done to obtain a uniform and smooth surface. The specimens were loaded between two steel plates for the compression test. Two roller supports were used for the splitting test. Three cubic samples for each approach and three cubic samples for each cutting angle were tested. The test was performed with a loading rate of 0.5 mm/min for the compression test and 0.3 mm/min for the splitting test. The splitting strength is defined as Eq. (1):

$$S = \frac{2P}{\pi D^2} \tag{1}$$

where S is splitting strength (MPa), P is peak load (kN), and D is the length of cube.

3.3. Four-point bending test

Four-point bending test was conducted using a universal testing machine (WDW-10E microcomputer-controlled electronic). Five samples were tested for each cutting direction to secure proper reproducibility of the results. The loading and support spans were 100 mm and 300 mm, respectively. A constant displacement rate of 0.5 mm/min was applied. Four-point flexural strength can be determined by Eq. (2):

$$F = \frac{PL}{bd^2} \tag{2}$$

where F is flexural strength (MPa), P is peak load (N), L is support span (mm), b is specimen width (mm), and d is specimen depth (mm).

3.4. Strain field and crack width analysis

DIC technique was applied to visualize the strain field and analyze the cracking behavior of specimens under uniaxial tension and compression tests [10]. For DIC analysis, white base paint and random black speckles were applied to the specimen surface, as shown in Fig. 3. The digital images were captured every 3 s during the test using a Canon EOS 80D camera with a spatial resolution of 2976 × 1984 pixels and a graphic resolution of 5.9 megapixels. The distance from the sample center to the camera was set as 656 mm for all tests. This leads to the full visibility of the specimen. The acquired images were post-processed using Match ID 2021 software. A subset size of 21 × 21 pixel^2 and a step size of 10 pixels were selected for the analysis. The average number of cracks and crack spacing were measured using ImageJ software by dividing the cracked zone length by the number of cracks. The cracked zone length was assessed from photos as the distance between the two adjacent cracks [44].

3.5. SEM imaging and image segmentation

To quantify the fiber alignment degree caused by different casting approaches, SEM images were taken under the backscattered electronic (BSE) microscope mode, as shown in Fig. 5. For bending test, four beam specimens were cut from each O-ECC slab in different directions (see Fig. 2a). After bending test, small specimens of 10 × 15 × 5 mm were then cut out from each beam specimen for the BSE investigation. The cut positions were far away from the loading zone (see Fig. 4). Then, the cut specimens were vacuum soaked using epoxy resins and kept for 24 h under room condition. Afterwards, all specimens were ground and polished until a smooth surface was obtained. After each polishing step, samples were soaked in absolute ethanol, and an ultrasonic bath was used to remove any residual dust. A magnification of 50× was utilized to reveal the fiber within the matrix [45]. Under this setup, the image covers an area of 2.38 mm × 1.91 mm with a resolution of 1.85 μm/pixel. For each case, five images from different positions (blue dots) on the cross-section were taken (see Fig. 4). The acquired microscopy images were then analyzed using ImageJ software to distinguish the PVA fiber from the surrounding ECC matrix, a process known as image segmentation. To improve the segmentation process, microscope images can be filtered first to sharpen the fiber boundaries and reduce noise. The fiber inclination angle θ of each specimen was then calculated by calculating the minor and major axes of each fiber's cross-section, as shown in the following section. The image processing analysis is described in detail in Ref. [42].

3.6. Fiber orientation analysis

After the image segmentation, the acquired data was used to characterize the features of fiber alignment. The number of fibers N_f per unit area is defined as the following equation

$$N_f = \frac{N_t^f}{A} \tag{3}$$

where N_t^f is the total number of fibers counted in the acquired image, A is the total image area.

The fiber inclination angle can be determined according to its projected cross-section on the captured image [46]. The cross-section of the fibers can be shaped in three forms at the plane, namely circle, elliptical and rectangular. The major axis and minor axis of each projected cross-section can be used to quantify the fiber orientation angle using Eq. (4)

$$\theta = \cos^{-1}\frac{d_f}{l_f} \tag{4}$$

Table 5
Fiber orientation parameters of the F–O specimens at different cutting direction.

parameters	F–O				F-R
Fiber properties	Cutting direction angle				
	FC-0	FC-30	FC-45	FC-90	
Average Fiber Orientation	26.2°	36.7°	53.0°	64.6°	47.1°
Orientation factor	0.86	0.75	0.57	0.40	0.68
Distribution coefficient	0.64	0.54	0.52	0.61	0.53
Total Number of fibers	75	53	39	36	51
Number of fibers per unit area N_f	17	12	8	7	11

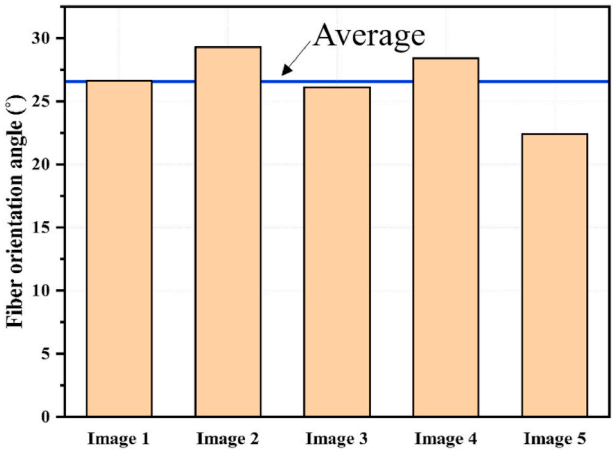

Fig. 6. Fiber orientation angle at different zones for FC-0 specimen.

where θ is the fiber orientation angle, defined as the angle between the fiber axis and the normal direction to the cut plane, d_f is the fiber diameter and represents the minor axis length of the fiber sectional image, l_f is the major axis length of the fiber.

To investigate the variance of fiber orientation angle, an orientation factor α was introduced using Eq. (5)

$$\alpha = \frac{1}{n}\sum_{i=1}^{n}\cos\theta_i \tag{5}$$

where n is the total number of fibers in the acquired images, θ_i is the orientation angle of fiber i. When $\alpha = 1$, all the fibers parallel to the reference direction, while $\alpha = 0$, all the fibers are perpendicular to the reference direction.

To assess the difference of fiber distribution within matrix, fiber distribution factor η was determined using Eq. (6)

$$\eta = \exp\left(-\sqrt{\frac{\sum\left(\frac{X_i}{X_{ave}}-1\right)^2}{n}}\right) \tag{6}$$

where X_i is the number of fibers in ith image, X_{ave} is the average number of fibers in all images, and n is the number of images.

4. Results and discussion

4.1. Fiber orientation characteristics

Fig. 5 presents the BSE images of the samples cut from the F–O slabs at 0°,30°,45°,90° inclined degree with respect to the flow direction and F-R specimen. The black dots represent the cross-section of PVA fibers, while the remaining grey regions indicate the cementitious matrix [14]. The fiber orientation angle, orientation factor, and the number of fibers for each specimen are summarized in Table 5. In the FC-0 specimen, most fibers tend to be circular and uniformly distributed (see Fig. 5). As the cutting angle increases, the projected cross-section shifts from circular to ellipse, as observed in FC-30 and FC-45 specimens. Clearly, the greater the cut angle, the greater the projected area. Most fibers in FC-90 specimens tend to have a flattened ellipse and an approximately rectangular shape. Five images from different positions on the cross-section were taken for each case. Fig. 6 shows the fiber orientation angle calculated from different positions for FC-0 specimens. The variance coefficient is smaller than 0.1. This means that the fiber alignment is more or

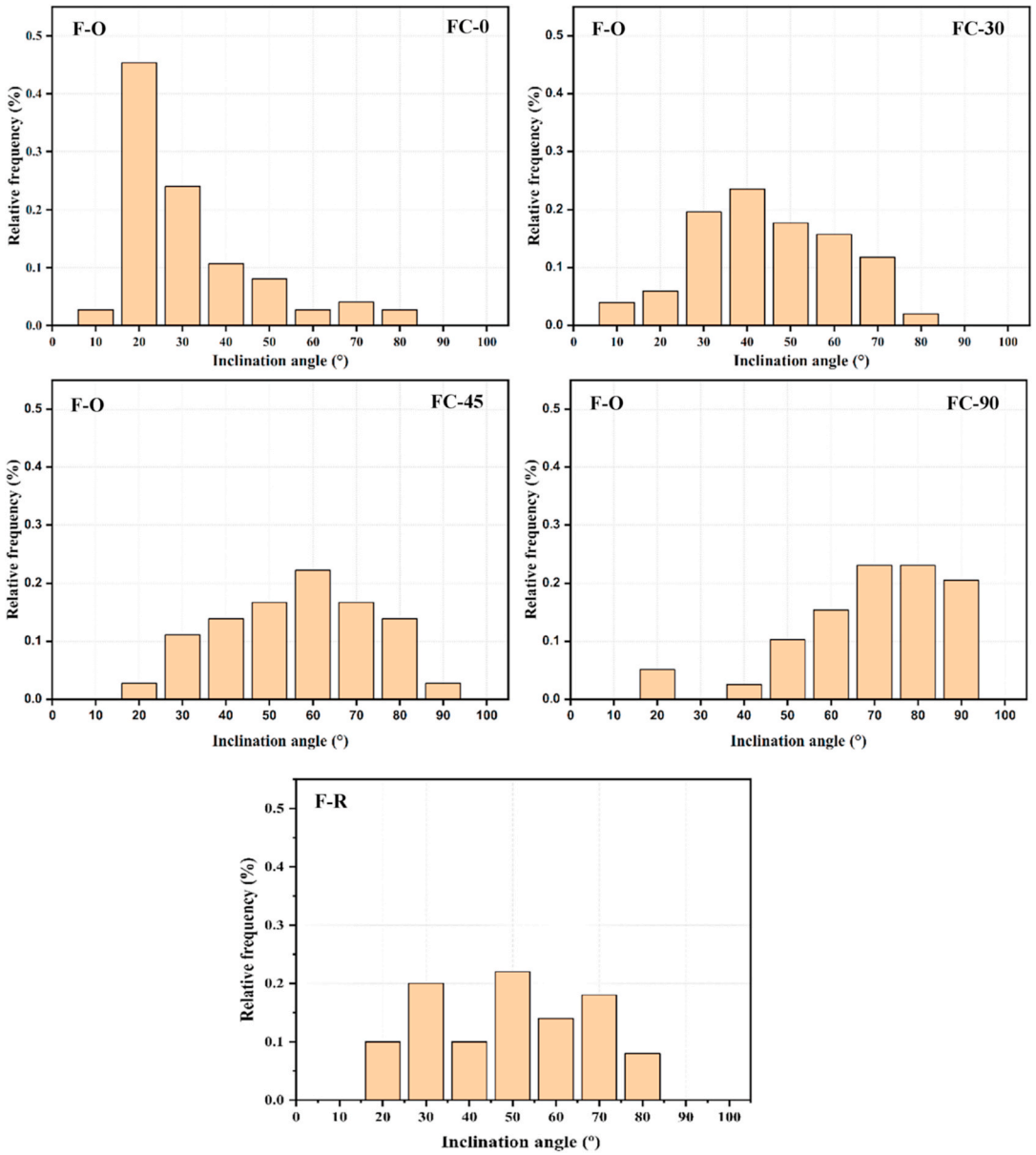

Fig. 7. Relative frequency distribution of the fiber inclination angle at different cutting direction of the F–O and F-R slabs.

less the same along the cross-section, and the calculated orientation factor is representative. Besides, a higher fiber distribution coefficient indicates a more uniform fiber distribution. The fiber distribution coefficient of FC-0 is 20.7% higher than that of F-R, indicating that the extrusion approach indeed enhances the fiber distribution in ECC.

Furthermore, the fiber orientation factor α of the FC-0 specimens were 0.86, which is about 15%, 51%,115%, and 27% greater than the FC-30, FC-45, FC-90, and F-R specimens, respectively. The larger the fiber orientation factor, the smaller the angle between the fiber and the perpendicular direction to the cut section. Similar observation was found by Bi et al. [47]. The findings demonstrate that the FC-0 specimens provide a better fiber orientation and more fibers number in the matrix cross-section. This can be attributed to the flow-induced method where the fibers are aligned with the flow direction, leading to a higher number of fibers per unit area. In this case, the fiber content required can be reduced while maintaining the mechanical properties of the ECC mixture. This would be an important step towards decreasing the production cost of the ECC.

The relative frequency distribution of fiber inclination angle is shown in Fig. 7. It is clear that the fiber angle is centralized within the range of 10°-30° for FC-0 specimens, which occupies about 69% of the total amount. This confirms that the flow-induced casting approach is an effective way to enhance fiber alignment. In terms of the FC-30, FC-45, FC-90, and F-R specimens, the relative frequency of the inclined fiber angle exhibits a broad distribution, where 61%, 54%, 67%, and 53% of the total amount was mainly within the

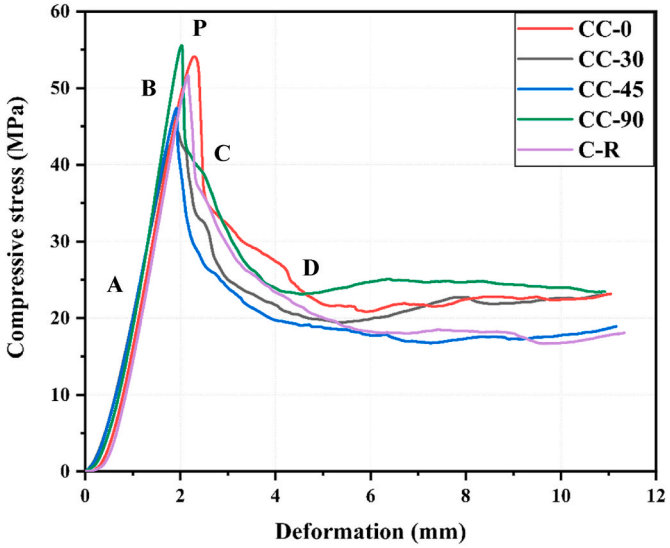

Fig. 8. Compressive stress-deformation curves of C–O at different fiber angle and C-R specimens.

Table 6
Compression strength and fracture energy of the C–O at different cutting direction and C-R specimens.

Specimen name	Compression strength (MPa)	Fracture energy (N/mm)
CC-0	54.0 ± 1.43	34.6
CC-30	44.2 ± 0.86	34.0
CC-45	47.4 ± 0.75	29.0
CC-90	55.6 ± 0.92	38.1
C-R	51.4 ± 1.69	30.2

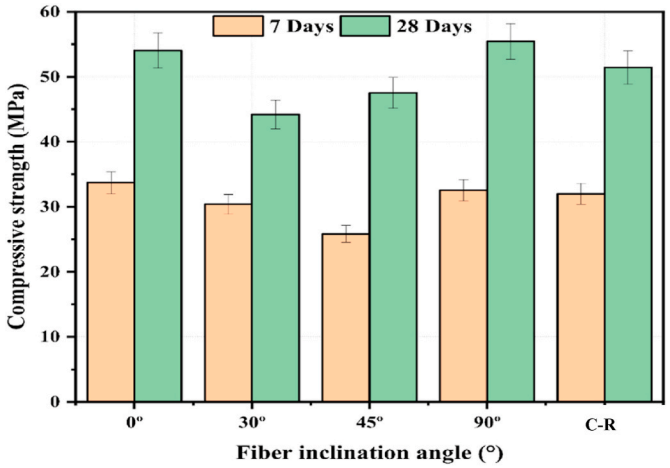

Fig. 9. Compressive strength of the flow induced casting method at different fiber inclination angle and conventional methods of ECC.

range of 30°-60°, 40°-70°, 60°-90°, and 40°-70°, respectively, see Fig. 7. The results show clear evidence that the fibers within the slab differ in orientation. This indicates that fiber distribution and orientation highly depend on the casting approach [48,49]. Noteworthy, during the extrusion of the ECC through the nozzle, the wall effect and the nozzle's shape enhance the fiber alignment in the flow direction [37,50].

4.2. Compression behavior

Fig. 8 shows the compressive stress-deformation curves of the cube specimens at different fiber inclination angles and C-R specimens. The stress-deformation curve can be divided into four regimes: a linearly ascending regime, a short non-linear ascending

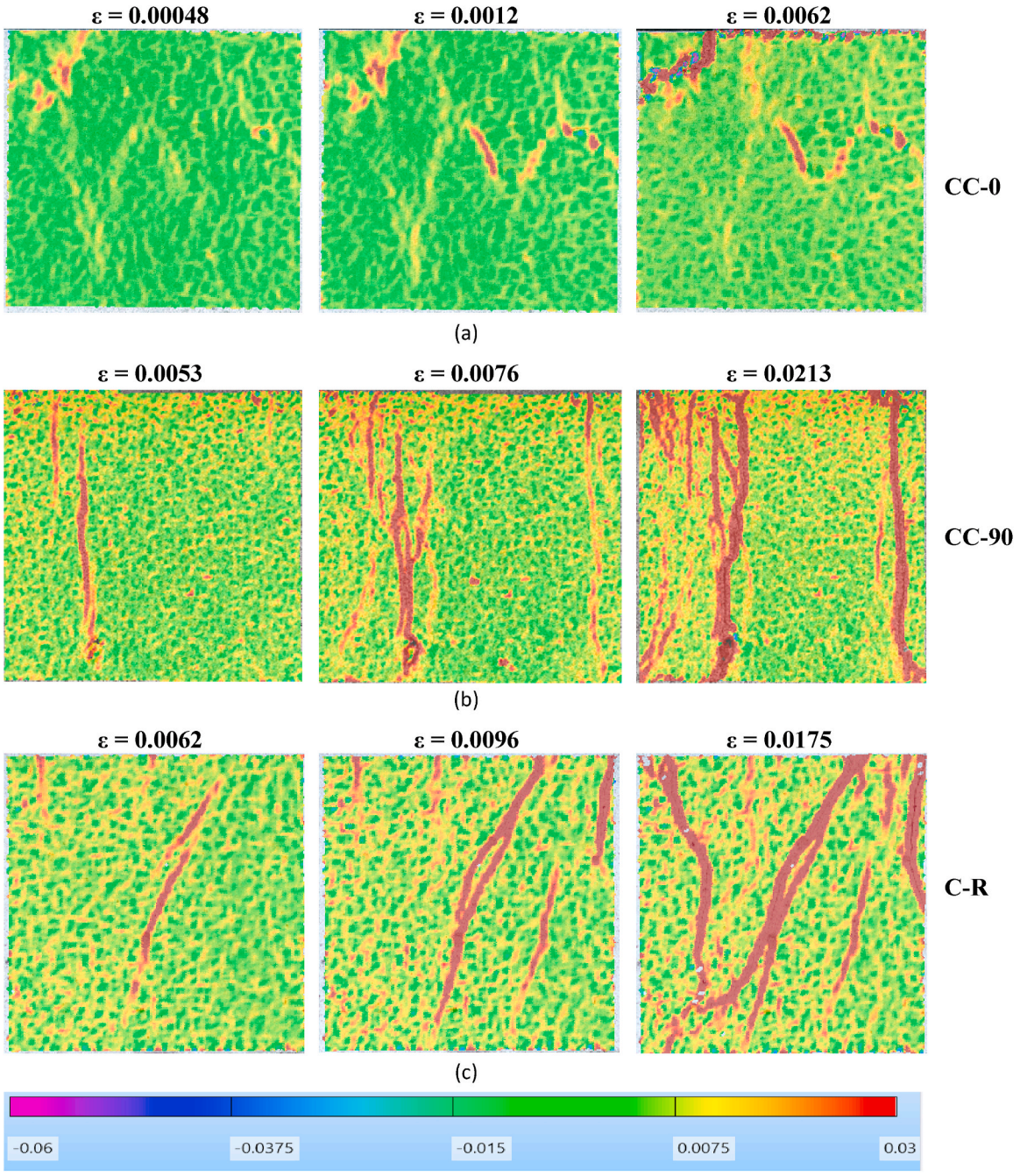

Fig. 10. The strain field and failure pattern of (a) CC-0, (b) CC-90 and (c) C-R specimens (The color bar represents the strain, the negative corresponds to the compressive strain and positive means tensile strain). (For interpretation of the references to color in this figure legend, the reader is referred to the Web version of this article.)

regime, a descending regime, and a residual state regime. The linearly ascending region A referred to the elasticity modulus of ECC grown under the elastic deformation, followed by a short non-linear ascending regime B before the peak load. This non-linearity ascending curve results from various deformations as the initial closure of pores and microcracking initiation caused by the lateral expansion of the specimen [51]. The fibers act as barriers against the crack widening. Afterwards, the main crack is formed at the peak load (point P). In the descending regime C, different post-peak behavior was observed for different specimens, where the slope of this regime increases with the increase of fiber inclination angle relative to the load direction. In this regime, the matrix gradually loses its load-resisting ability with increasing deformation. Here, cracks propagate and coalesce in irregular patterns up to the boundaries of the specimen. Then, a gradual decrease of stress with increasing the deformation continues until the residual state D. This is followed by

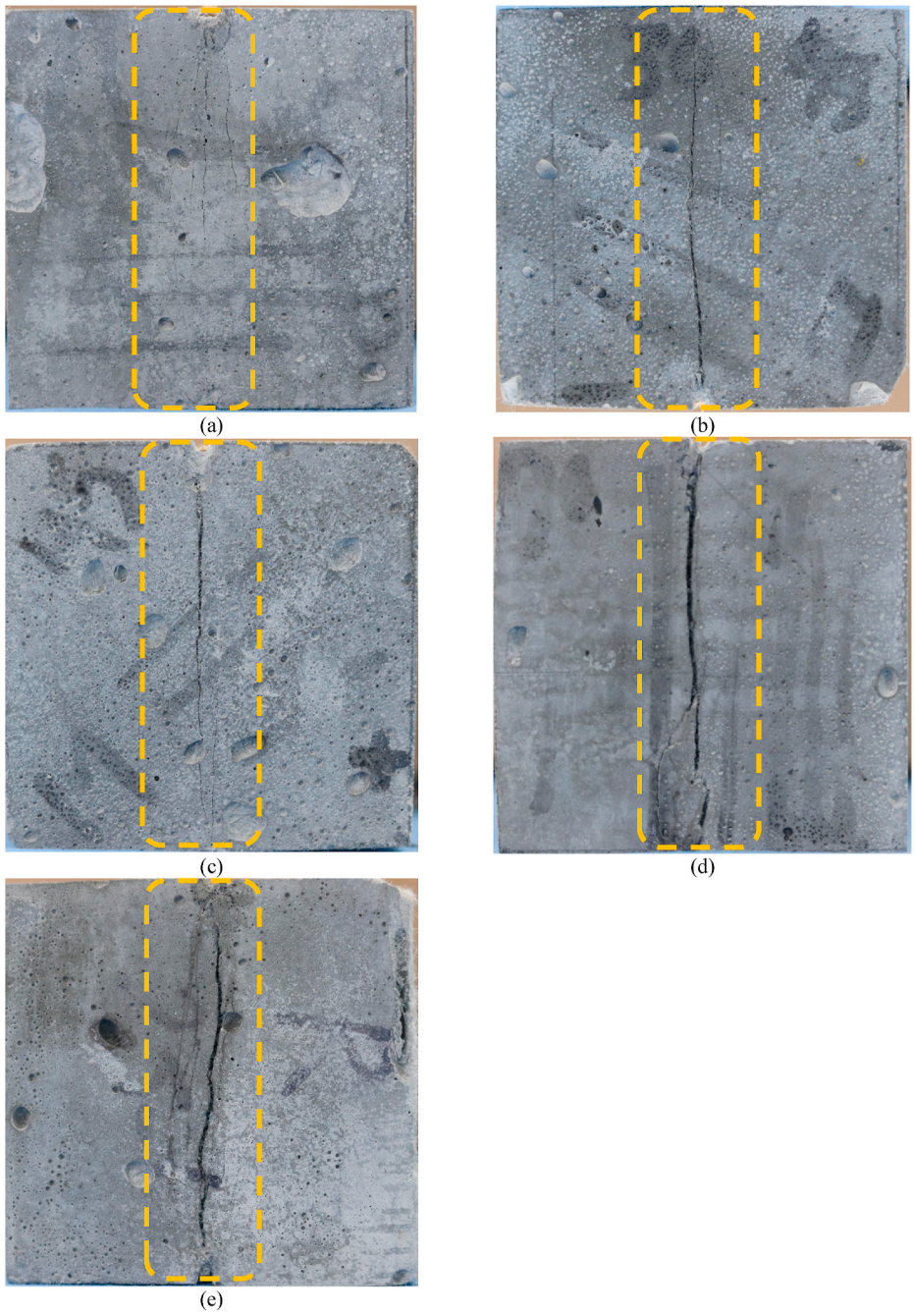

Fig. 11. Splitting strength of specimen at different fiber angle: (a) SC-0; (b) SC-30; (c) SC-45; (d) SC-90and the (e) S-R specimens.

Table 7
Splitting strength of the S–O and S-R specimens.

Casting method	Cutting direction angle	Splitting strength (MPa)
S–O	SC-0	2.91 ± 0.18
	SC-30	2.44 ± 0.14
	SC-45	2.63 ± 0.09
	SC-90	2.59 ± 0.12
S-R		2.53 ± 0.15

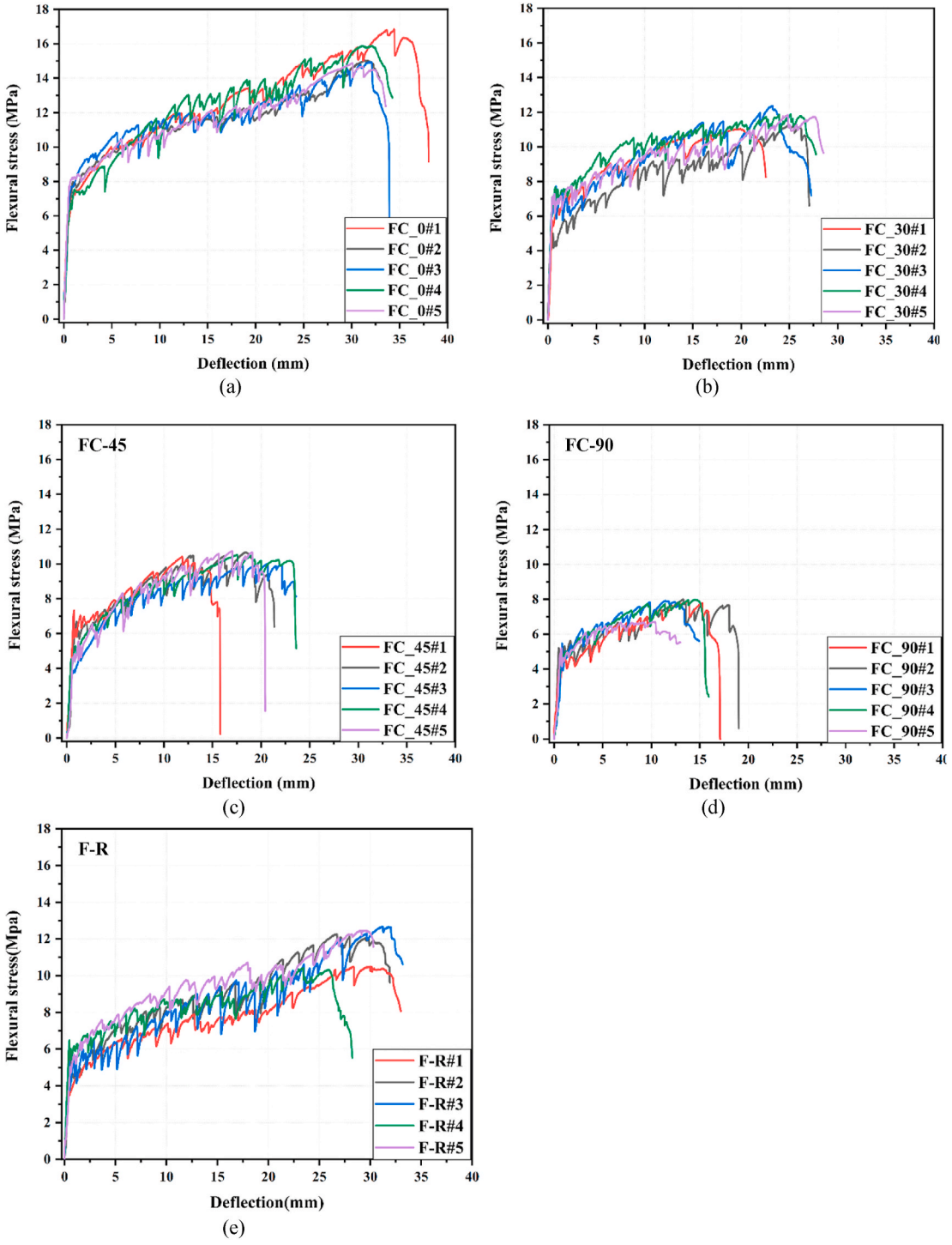

Fig. 12. Flexural stress-deflection curves of the F–O specimens at different cut direction: (a)0°; (b)30°; (c) 45°; (d) 90° and (e) F-R specimens.

the curve's flattening. In this regime, the stress-deformation curves of the C–O specimens with different cutting directions exhibit more ductile behavior, where the stress curves remain almost constant with increasing the deformation. Compared to the C-R specimens, the stress curve gradually decreases with increasing the deformation. Table 6 presents the fracture energy of ECC specimens at different fiber orientations. The fracture energy is defined as the post-cracking energy absorption ability of the material, it represents the energy that the material will absorb during failure [52–54]. In the current study, the area under the post-peak regime of the stress-deformation curve was used for the fracture energy calculation and end of the deformation was taken as 11 mm. The fracture energy of the CC-0 and

Table 8
The mechanical properties and crack parameters of the F–O specimens at different fiber angle and F-R specimens under four-point test.

Mechanical properties	F–O				F-R
	Cutting direction angle				
	FC-0	FC-30	FC-45	FC-90	
First crack strength (MPa)	6.10 ± 0.58	5.70 ± 0.77	5.20 ± 1.18	4.80 ± 0.39	5.06 ± 1.1
Ultimate flexural strength (MPa)	15.50 ± 0.94	12.20 ± 0.57	10.47 ± 0.28	7.70 ± 0.55	11.67 ± 0.89
Mid-span deflection (mm)	32.92 ± 1.63	23.64 ± 2.19	17.11 ± 3.25	12.73 ± 1.7	28.34 ± 2.1
Number of cracks	47 ± 5	36 ± 3	24 ± 3	13 ± 2	41 ± 2
Crack spacing (mm)	3.89	4.22	7.21	11.69	4.28

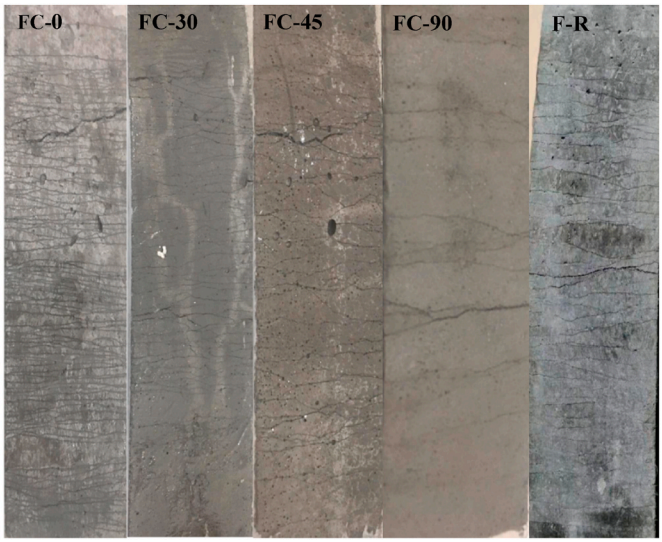

Fig. 13. Crack pattern of the F–O specimens at different cut direction and F-R specimens after four-point bending test.

CC-90 are 34.6 N/mm and 38.1 N/mm which are 14.55% and 26.16% greater than C-R specimens. This improvement can be attributed to the contribution of fiber alignment with the load direction to the failure resistance, where the deformations on the existing cracks continue to propagate under almost a constant stress level. Furthermore, the fiber alignment also decreases the fiber distances leading to higher fracture energy [55].

Fig. 9 presents the compressive strength of both flow-induced at different fiber inclination angles and conventional casting methods of the ECC specimens. Table 6 summarizes the average compressive strength of three cubes tested for the C–O specimens at the different cutting directions and C-R specimens at 7 and 28 curing days. The compressive strength of the C–O specimens at the CC-0 and CC-90 cutting direction relative to the load direction was higher than the C-R specimens (see Fig. 9). This improvement can be attributed to the mechanical pressure caused by the auger rotation during the extrusion process which enhances the compaction of the mixture leading to an increase in the compressive strength [56]. Furthermore, the positive effect of controlling the fiber orientation on the compressive strength is the fiber's ability to confine the concrete specimen under uniaxial loading [57]. The applied load produces lateral expansion of the specimen, creating tensile and shear forces on the specimen's lateral surfaces. The oriented fibers resist the tension and shear forces more than the randomly distributed fibers [57]. Increasing the number of oriented fibers within the cementitious matrix in the horizontal or vertical direction leads to confining the specimen in the transversal direction, which reduces the transversal deformation of the cementitious specimen, enhancing its compressive strength. The compressive strength of the flow-induced specimens at the CC-0 and CC-90 was 54.0 and 55.6 MPa, which is 5.05% and 8.03%, higher than the conventional specimens. Thus, the uniaxial compressive behavior is sensitive to the fiber alignment [58]. Fiber misalignments related to the load direction significantly lower the composite compressive strength. The composite is locally subjected to longitudinal stress and transverse shear stress due to the compressive composite stress decomposition. As the fiber angle in relation to the loading direction increases, the longitudinal stress decreases, while the transverse shear stress increases [59].

Depending on the direction of the PVA fiber, the compressive strength of cubes that cut from the C–O prismatic specimen at different cutting angles [0°, 30°, 45°, 90°] varied by up to 19%, about 10.6 MPa (see Fig. 9). In this regard, the unidirectional of the fiber in the compression loading direction turned out to be critical. The compressive strength obtained from the C–O specimens was 54.0 and 55.6 MPa, for fiber orientation degree [0°, 90°]. While it was 44.2 and 47.4 MPa for the specimens with [30°, 45°] fiber orientation degree, respectively. The reduction in compressive strength at fiber orientation degree [30°, 45°] is due to the effect of the shear friction caused by the applied load in the fiber/matrix interface, which leads to poor interfacial bonding resulting in matrix

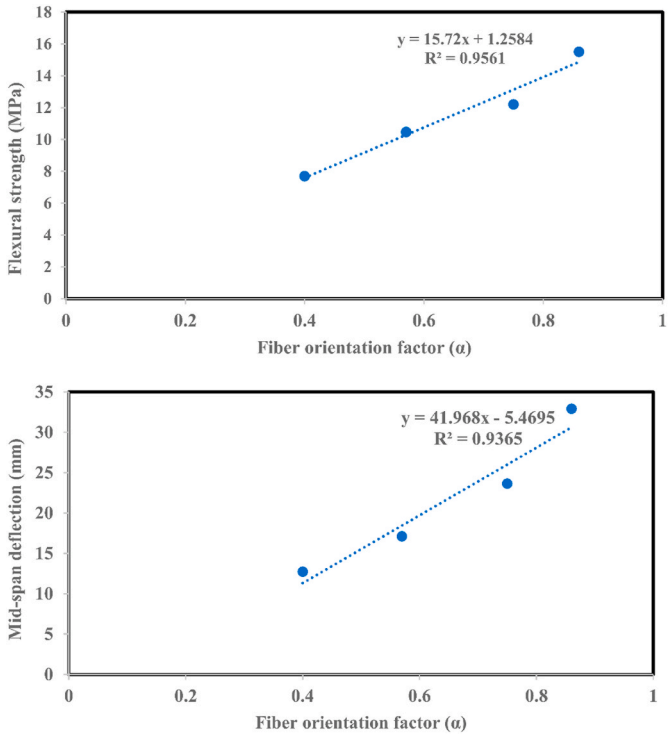

Fig. 14. Relations between flexural strength and mid-span deflection at different fiber orientation factor.

failure. Similar observations were reported in Ref. [60].

The DIC strain field as a color map overlaid on the surface and the failure patterns of the CC-0 and C-R specimens are shown in Fig. 10. It was observed that the strain field of the CC-0 and CC-90 specimens is relatively uniform. In addition, the failure occurred along the longitudinal direction of the fiber, where cracks follow the fiber direction and are relatively arrested in the transverse direction of the fiber (see Fig. 10a and b). Furthermore, the crack pattern is finer and more homogeneously distributed with the fiber direction, indicating a better internal stress distribution on the surface. Compared to the C-R specimens, the strain field is shown unevenly distributed, and the failure took place at all specimen sides with the formation of inclined cracks. In addition, the crack patterns are wider and heterogeneous distributed, where the vertical cracks begin from the top at an inclined angle and are less dominant (see Fig. 10c). According to Riedel et al. [61], the unidirectional fiber alignment improves the compressive strength of ultra-high-performance concrete more than random fiber.

4.3. Splitting behavior

Fig. 11 shows splitting cracks of S–O specimens at 0°, 30°, 45°, and 90° cutting directions perpendicular to the load direction, and the S-R specimens. The peak load and splitting strength of ECC specimens for both casting methods are listed in Table 7. In general, the specimens broke into two portions due to the brittle cracking behavior.

On the other hand, fiber orientation plays an important role in enhancing the splitting strength and specifying the crack pattern [62]. Different failure patterns appeared on ECC specimens, see Fig. 11. Local splitting cracks grow on both sides of the main splitting crack at a certain load, where the fiber bridging the cracks redistributes the tensile stress of the cracked ECC matrix. The splitting strength of the S–O specimens at SC-0 is 2.91 MPa which is 1.15 times that of the S-R specimens. In addition, paralleled local cracks on both sides of the main splitting crack are observed for the SC-0 specimen, while only one crack is observed for the S-R specimens. In the case of the SC-30 and SC-45 specimens, one local crack parallel to the main splitting crack in the SC-30 specimen is developed, while multiple cracks appeared parallel to the main splitting crack in the SC-45 specimen. In the case of the SC-90 specimens, a local crack branching the main splitting crack was developed. The improvement of the splitting strength in the SC-0 specimens may be attributed to the effect of fiber direction relative to the tensile load. In addition, the embedded effective length increases as the inclination fiber angle are smaller with the direction of the load [63], which enhances the splitting strength and crack propagation. Furthermore, the splitting strength of SC-45 and SC-90 specimens enhances when compared to S-R specimens. This can be attributed to the unidirectional fiber distribution which provide sufficient bonds between the fiber and cement paste more than random fiber distribution, enhancing the concrete strength [53].

4.4. Flexural performance

The flexural stress-deflection curve of the F–O specimens at different cut directions (0°, 30°, 45°, and 90°) and the F-R specimens

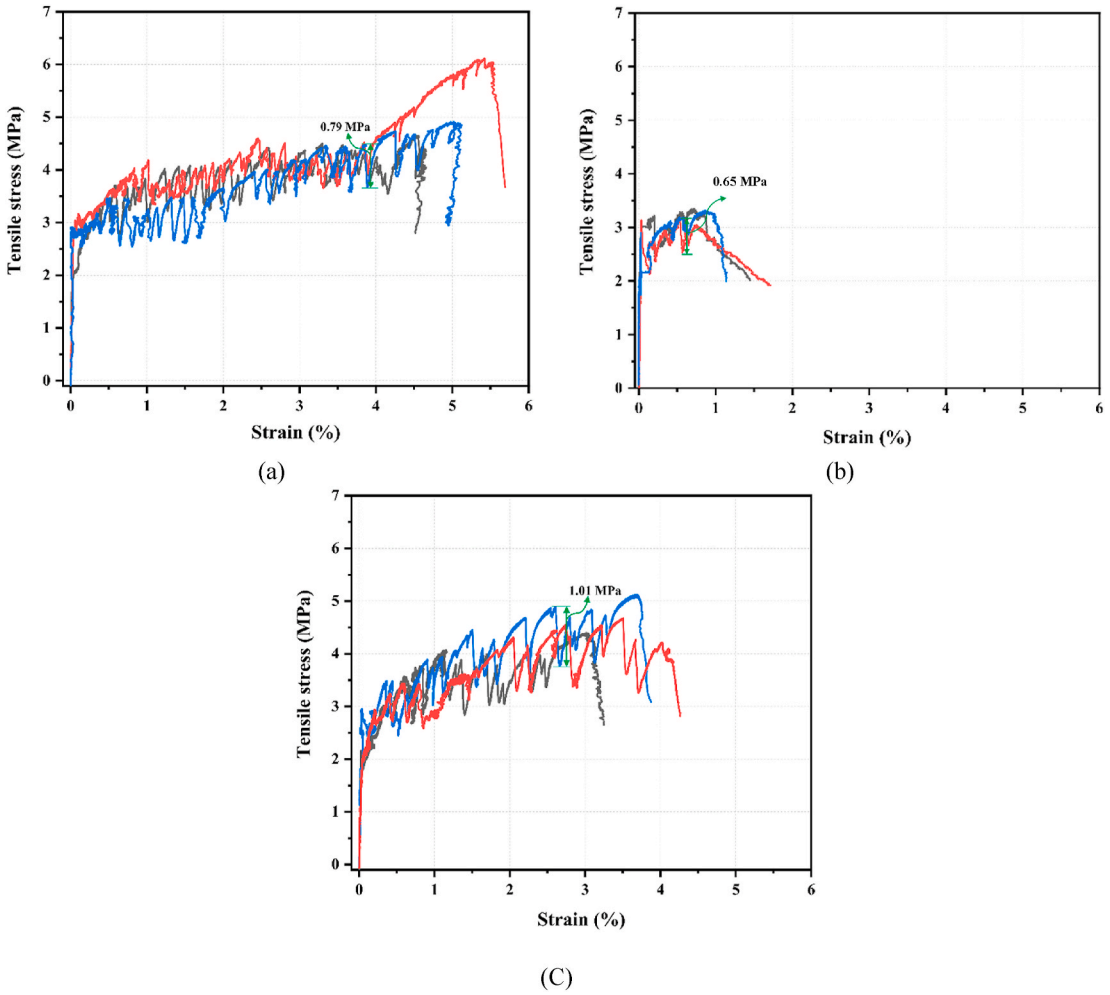

Fig. 15. The tensile stress-strain curves of the (a) T-0, (b) T-90, and (C) T-R specimens.

Table 9
The mechanical tensile properties of the T-0 and T-R specimens at 28 days.

Mechanical properties	T-0	T-90	T-R
First cracking stress (MPa)	2.91 ± 0.25	2.66 ± 0.56	2.67 ± 0.44
Peak stress (MPa)	5.20 ± 0.78	3.28 ± 0.087	4.55 ± 0.38
Strain capacity (%)	5.00 ± 0.45	0.85 ± 0.3	3.51 ± 0.35
Number of cracks	23 ± 3	7 ± 3	15 ± 4
Average crack width (μm)	72 ± 23	108 ± 78	118 ± 18

are plotted in Fig. 12. The first crack strength, ultimate flexural strength, mid-span deflection crack number, and crack spacing for each condition are summarized in Table 8. It is evident that all specimens exhibit deflection-hardening behavior. However, the deformability and bearing capacity are different (see Fig. 12). This can be attributed to the varied crack-bridging capacity caused by the different fiber orientation [24,64]. At the beginning, the mid-span deflection increases linearly under the flexural loads. When reaching the end of the linear regime, a sudden drop occurs. It can be attributed to the first crack formation [42,65]. The point just before the drop is therefore defined as the first crack strength. With fiber angle relative to the cast direction increasing, the first crack strength gradually reduces. As it has been pointed out by Refs. [66,67], the influence of fiber is limited on the first crack strength because the matrix strength dominates the stress. Specifically, the average first cracking strength of the FC-90 specimens is 4.8 MPa, which is 21.3% lower than FC-0 specimens. This is in accordance with [14]. In comparison, the first crack strength of the F-R specimens is 5.06 MPa which is 17% lower than the F–O specimens in the case of the FC-0 cutting direction with the flow direction.

After the first cracking point, the flexural stress-deflection curves continue rising until the ultimate flexural stress. At this point, the main crack localizes. In this stage, different deflection-hardening behaviors accompanied by the formation of multiple cracks are

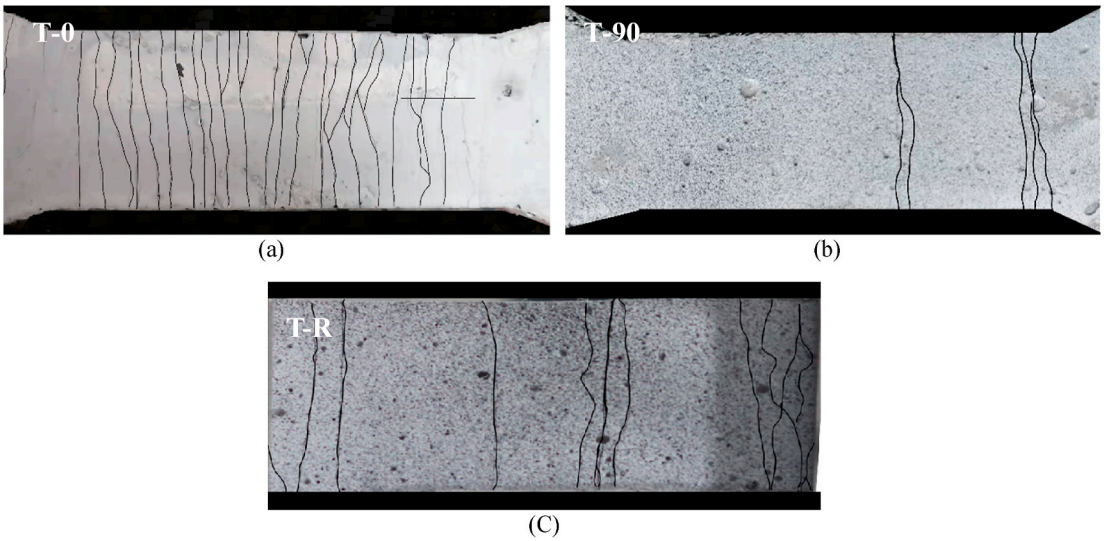

Fig. 16. Crack patterns of (a) T-0, (b) T-90, and (c) T-R specimens.

observed in each group. This is due to the various crack-bridging capacities caused by the fiber distribution and orientation [14,68]. The deflection-hardening curves of the FC-0 specimens exhibit more fluctuations than the others, indicating that more cracks are formed. This is because most fibers are aligned to the tensile load direction, which enhances the fiber bridging strength. Therefore, a significant amount of stress can be transferred from the matrix to the fibers, enhancing the crack growth restriction. Ge et al. [42] pointed out that the smaller the inclined angle between the fiber and tensile stress, the greater the fiber bridging stress. Consequently, higher flexural strength and deflection capacity were obtained. In contrast, with the larger inclination angle of the fiber relative to the tensile stress, the fibers are undergoing higher stress caused by the snubbing effect. Therefore, the fiber is more likely to rupture, which leads to lower strength [2]. The ultimate flexural stress of the FC-0 specimen was 15.5 MPa which is about 27%, 48%, 101%, and 32.8% greater than the FC-30, FC-45, FC-90 specimens, and F-R specimens, respectively. This corresponds to different mid-span deflection, where the deflection is 32.92 mm for the FC-0 specimens, which is 39%, 92%, 159%, and 16% greater than the FC-30, FC-45, FC-90 specimens, and F-R specimens, respectively. The improved deflection-hardening in the FC-0 specimen ascribes to the flow-induced effect on the fiber inclination. During this stage, fibers are aligned with the flow direction. This results in a greater effective embedded length, which mainly leads to enhancing the fiber bridging strength and overall performance of ECC [66,69,70].

Fig. 13 shows different crack patterns of the F–O specimens with different cutting directions and F-R specimens. The crack distribution of the FC-0 specimens was more uniform than the others. It is also noticed that the crack number increases, and the crack spacing decreases as decreasing the inclined fiber angle relative to the load direction. The number of cracks increases from 13 cracks to 47 cracks, while the crack spacing reduces from 11.69 mm to 3.89 mm for the FC-90 and FC-0 specimens, respectively (see Table 8). Compared to F-R specimens, the number of cracks and crack spacing were 41 and 4.28 mm, respectively. The improvement of the FC-0 specimens indicates the positive influence of the fibers, especially with the small inclination angle on the crack widths and crack spacings as well as on the deformation behavior.

ECC with better fiber orientation (larger fiber orientation factor α) exhibits higher flexural strength and deflection. Fig. 14 depicts a relationship between flexural strength and mid-span deflection at various fiber orientation factors. Flexural strength and deflection increase linearly as the fiber orientation factor increases. Results of flexural strength and deflection exhibit good linear correlation with the fiber orientation factor, which can be expressed by a quadratic function ($R^2 > 0.95$) and ($R^2 > 0.93$), respectively.

4.5. Uniaxial tensile behavior

The uniaxial tension stress-strain curves of the T-0, T-90, and T-R specimens are plotted in Fig. 15. The stress-strain responses demonstrate a noticeable difference in strain-hardening behavior for different types of specimens. The first crack strength, ultimate tensile strength, strain capacity, crack number, and crack width are tabulated in Table 9. At the beginning, the tensile stress-strain curves rapidly increase under elastic deformation until the first crack is formed. The first cracking strength of the T-0 specimen is 2.91 MPa, which is 9.3% and 8.9% higher than T-90 and T-R specimens, respectively. The limited difference in the first cracking strength in the tensile test is similar to the observation in the flexural test, which may be attributed to the fact that it is the matrix that mainly governs the tensile behavior of the cementitious composite before cracking [64]. While the fiber orientation and distribution have a quite limited effect on the first cracking stress [71].

After the first crack, the tensile stress curves increase with the development of subparallel cracks, which contribute to increasing the strain and load bearing capacity until the peak load. At this point, a localized crack is formed, leading to the failure. The ultimate tensile strength of the T-0, T-90 and T-R specimens are 5.2 MPa, 3.28 MP and 4.55 MPa, and their corresponding tensile strain reaches 5%, 0.85% and 3.5%, respectively. The stress and strain increment of the T-0 specimens are over 14% and 42% compared to T-R

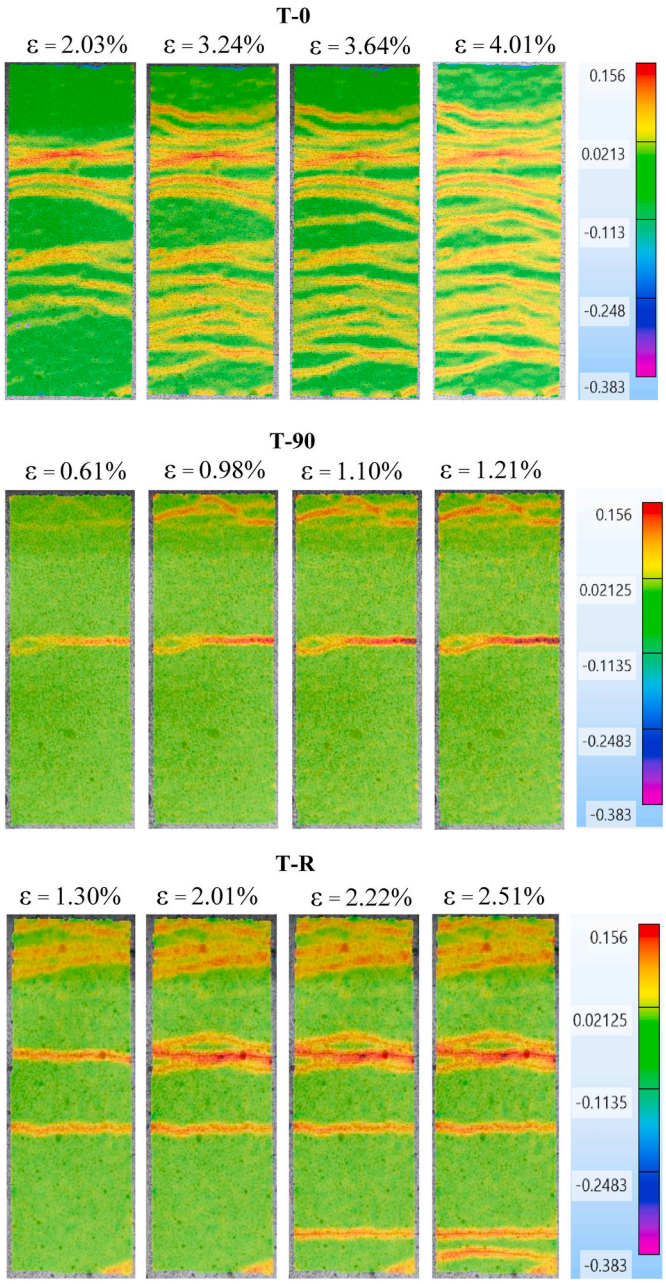

Fig. 17. DIC strain fields and crack patterns of the T-0 and T-R specimens at different strain level (The color bar represents the tensile strain). (For interpretation of the references to color in this figure legend, the reader is referred to the Web version of this article.)

specimens, respectively, and 59% and 488% higher than T-90 specimens, respectively, indicating a strong effect of the fiber orientation on the stain-hardening behavior, which is usually governed by the fiber bridging capacity [24].

The magnitude of stress fluctuation on stress-strain curves is mainly determined by matrix strength and fiber bridging capacity [72]. The stress fluctuations along with the whole loading stage are shown in Fig. 15. A fine crack corresponds to minor stress fluctuation in the stress-strain curve, enhancing the strain-hardening behavior, while a large crack corresponds to considerable stress fluctuation. During crack propagation, the maximum stress drops of the T-0 specimens was 0.79 MPa, while it was 1.01 MPa for T-R specimens. Due to the fiber alignment enhancement by the flow-induced method, the fiber bridging capacity is enhanced to transfer the loads to the matrix, leading to formation of more fine cracks. Fig. 16 presents the crack patterns of the T-0, T-90 and T-R specimens. The difference in tensile behavior indicates that the fiber orientation depends strongly on the casting method and dramatically influences the stain-hardening behavior. In contrast, the matrix had a limited contribution to the tensile softening behavior [64].

Fig. 17 shows the DIC strain fields and crack pattern of the T-0 and T-R specimens at different strain levels, namely ($0.5\varepsilon_t$, $0.8\varepsilon_t$.

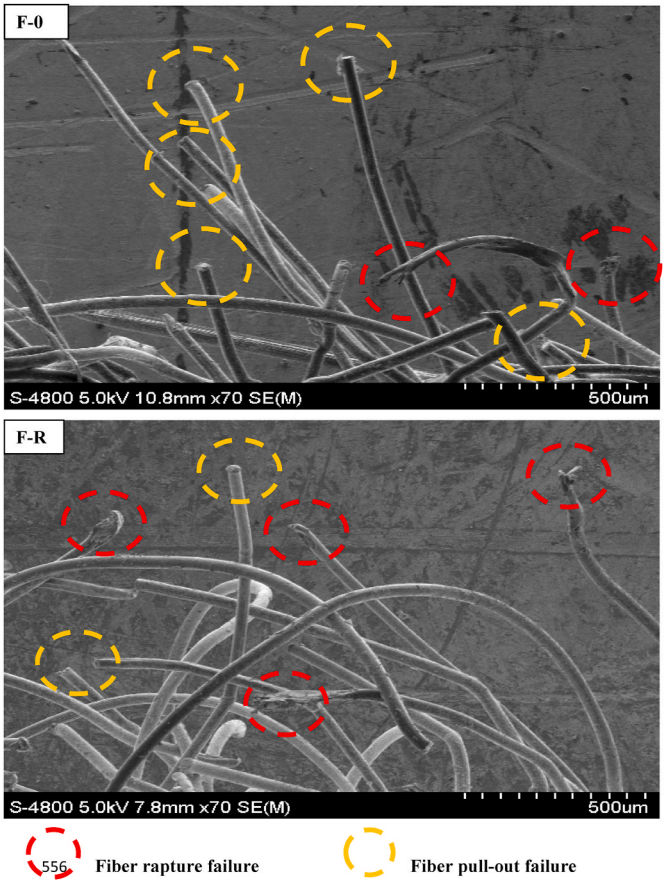

Fig. 18. SEM photographs of the fiber failure modes for the F-0 and F-R specimens.

$0.9\varepsilon_t$, and ε_t). ε_t is the ultimate tensile strain capacity of the ECC specimens. The color code represents the local tensile strain values. Note that the some of the tiny cracks are not visible in this strain filed. Nevertheless, multiple cracking behavior is observed for both specimens (see Fig. 17). As the tensile strain capacity increased, the number of cracks in the ECC specimens increased [73]. At the ultimate stage, saturated multiple cracking was achieved almost along with the T-0 specimens, while the cracks were concentrated in the upper and middle tension zone for the T-R specimens. This is attributed to the effect of fiber alignment in the load direction. It can also be noticed that the number of cracks in T-0 specimens was greater compared to T-R specimens. In T-0, 23 cracks form, which is 34% more than T-R (15 cracks). The number of cracks decreases to 7 for T-90. Using ImageJ software, the crack width was measured based on the original digital image shot at the ultimate tensile strain for each specimen. The crack was first segmented from the image and the crack width is measured based on the distance between each pair of crack lips. More details of this approach can be found in Ref. [74]. The average crack width of the T-0 specimens was 72 μm, while it was 108 μm and 118 μm for T-90 and T-R specimens, respectively.

4.6. SEM microscopy

The SEM micro-images of the fiber failure mode for the F-0 and F-R specimens under flexural test are shown in Fig. 18. A combination of pull-out and fiber rupture is observed in both specimens. The F-0 specimens exhibited more fiber pull-out failure than the F-R specimens due to the effect of the fiber alignment. In contrast, the fibers in F-R specimens are more prone to rupture failure. This is due to the fact the fiber in F-R was distributed randomly, leading to a significant variance in the fiber inclination angle relative to the load direction [75]. In addition, the apparent interfacial bond strength of the fiber/matrix reduces with increasing fiber inclination angle [76]. The occurrence of fiber rupture and matrix spalling increases with increasing fiber inclination angle related to the load direction [63], negatively affecting the fiber bridging strength [77]. Thus, the fiber alignment reduces the probability of fiber rupture, leading to enhancing the fiber bridging strength and tensile strength of the ECC matrix. Furthermore, the pull-out failure mode provides a larger ductility of the cementitious composite than fiber rupture failure [77]. This is confirmed by the current study.

5. Conclusions

In this study, the effect of fiber orientation on the mechanical properties of ECC made with different casting methods (Flow-induced and conventional methods) was investigated. It is found that when fibers are oriented with the load direction of ECC specimens,

improved fiber bridging strength and mechanical properties with finer crack width are obtained. The conclusions are as follows.

- The Flow-induced casting method achieves a higher degree of fiber alignment than the conventional method. For comparison, four patterns of fiber orientation were detected for the Flow-induced casting method and conventional method as well. The fiber orientation α of the FC-0 specimens reach 0.9, which is about 20%, 58%,125%, and 32% greater than the FC-30, FC-45, FC-90, and F-R specimens, respectively.
- Compared to random fiber distribution, increasing the number of oriented fibers horizontally or vertically improves the compressive strength and ductility of the post-peak behavior of ECC. Whereas increasing the number of oriented fibers with an inclined angle reduces the compressive strength of ECC. The compressive strength of the CC-0 and CC-90 specimens was 54.0 and 55.6 MPa, which is 5.05% and 8.03 %higher than the C-R specimens, respectively. In contrast, the compressive strength of the CC-30 and CC-45 specimens was 44.2 and 47.4 MPa, which is 16.36% and 8.57%lower than the C-R specimens, respectively.
- The flexural performance of the F-0 specimens shows an improvement over the F-R specimens according to the fiber inclination angle and casting method. The ultimate flexural stress of the FC-0 specimens was 15.5 MPa which is about 27%, 48%, 101%, and 32.8% greater than the FC-30, FC-45, FC-90 specimens, and F-R specimens, respectively. This is accompanied by larger deflection and more narrow cracks.
- The fiber orientation plays a prominent role and governs the response of ECC matrix under splitting load, where the splitting tensile strength increases with the fiber orientation angle perpendicular to the load decreasing. The splitting strength of the S–O specimens at the SC-0 cutting direction is 2.91 MPa, which is about 15% greater than the S-R specimen.
- The flow-induced casting method leads to restricting crack width development under uniaxial tension loading with increased deformation ability and crack number due to the effect of fiber orientation. The average crack width and crack number of the T-0 specimens were 72 μm with 23 cracks, while it was 118 μm with 15 cracks, and 108 μm with 7 cracks for T-R and T-90 specimens.

Author statements

Abdullah M. Tawfek: Investigation, Writing - original draft. **Zhi Ge:** Funding acquisition, Writing - review & editing. **Huaqiang Yuan:** Writing - review & editing. **Ning Zhang:** Writing - review & editing. **Hongzhi Zhang**: Funding acquisition, Methodology, Supervision, Writing - review & editing. **Yifeng Ling:** Funding acquisition, Supervision, Writing - review & editing, **Yanhua Guan:** Writing - review & editing. **Branko Šavija:** Methodology, Writing - review & editing.

Declaration of competing interest

The authors declare that they have no known competing financial interests or personal relationships that could have appeared to influence the work reported in this paper.

Data availability

Data will be made available on request.

Acknowledgements

This work was supported by the National Natural Science Foundation of China (No.52008234, 51978387), Taishan Scholars Foundation of Shandong Province (No. tsqn201909032), Natural Science Foundation of Jiangsu Province (No. BK20200235), and China Scholarship Council (2018GXZ024231).

References

[1] F. Nateghi-A, M.H. Ahmadi, A. Dehghani, Experimental study on improved engineered cementitious composite using local material, Mater. Sci. Appl. 9 (2018) 315–329, https://doi.org/10.4236/msa.2018.93021.
[2] C. Lu, C.K.Y. Leung, Cement and Concrete Research Theoretical evaluation of fi ber orientation and its effects on mechanical properties in Engineered Cementitious Composites (ECC) with various thicknesses, Cement Concr. Res. 95 (2017) 240–246, https://doi.org/10.1016/j.cemconres.2017.02.024.
[3] V.C. Li, On engineered cementitious composites (ECC), J. Adv. Concr. Technol. 1 (2003) 215–230, https://doi.org/10.3151/jact.1.215.
[4] B.F. Boukhoulda, E. Adda-Bedia, K. Madani, The effect of fiber orientation angle in composite materials on moisture absorption and material degradation after hygrothermal ageing, Compos. Struct. 74 (2006) 406–418, https://doi.org/10.1016/j.compstruct.2005.04.032.
[5] N.S. Berke, M.P. Dallaire, T.A. Durning, K.J. Folliard, A.V. Kerkar, Development of steels for improved performance in reinforced concrete, J. Mater. Civ. Eng. 9 (1997) 1–6, https://doi.org/10.1061/(ASCE)0899-1561(1997)9:1(1).
[6] K. Tosun-felekog, E. Gödek, A novel method for the determination of polymeric micro-fiber distribution of cementitious composites exhibiting multiple cracking behavior under tensile loading, Construct. Build. Mater. 86 (2015) 85–94, https://doi.org/10.1016/j.conbuildmat.2015.03.094.
[7] J. Qiu, E.-H. Yang, Effects of microbial carbonate precipitation on transport properties of fiber cement composites, J. Mater. Civ. Eng. 28 (2016), 04015204, https://doi.org/10.1061/(asce)mt.1943-5533.0001500.
[8] S. Hedjazi, D. Castillo, Heliyon Relationships among compressive strength and UPV of concrete reinforced with different types of fi bers, Heliyon 6 (2020), e03646, https://doi.org/10.1016/j.heliyon.2020.e03646.
[9] J. Gustavo, W. Reinhardt Parra-Montesinos Hans, A.E. Naaman, High Performance Fiber Reinforced Cement Composites, 2012.
[10] B.-T. Huang, J.-G. Dai, K.-F. Weng, J.-X. Zhu, S.P. Shah, Flexural performance of UHPC–Concrete–ECC composite member reinforced with perforated steel plates, J. Struct. Eng. 147 (2021), 04021065, https://doi.org/10.1061/(asce)st.1943-541x.0003034.
[11] Q. Wang, Y. Yi, G. Ma, H. Luo, Hybrid effects of steel fibers, basalt fibers and calcium sulfate on mechanical performance of PVA-ECC containing high-volume fly ash, Cem. Concr. Compos. 97 (2019) 357–368, https://doi.org/10.1016/j.cemconcomp.2019.01.009.
[12] K. Bilisik, H. Ozdemir, Multiaxis three dimensional (3D) carbon and basalt preforms/cementitious matrix concretes: experimental study on fiber orientation and placement by panel test, Construct. Build. Mater. 271 (2021), 121863, https://doi.org/10.1016/j.conbuildmat.2020.121863.

[13] J. Choi, B.Y. Lee, Bonding properties of basalt fiber and strength reduction according to fiber orientation, Materials 8 (1) (2015) 6719–6727, https://doi.org/10.3390/ma8105335.
[14] C. Ding, L. Guo, B. Chen, Orientation distribution of polyvinyl alcohol fibers and its influence on bridging capacity and mechanical performances for high ductility cementitious composites, Construct. Build. Mater. 247 (2020), 118491, https://doi.org/10.1016/j.conbuildmat.2020.118491.
[15] V.C. Lr, Effect of Fiber Inclination on Crack Bridging Stress in Brittle Fiber Reinforced Brttle Matrix Composites, 1992.
[16] S. Ranjith, R. Venkatasubramani, V. Sreevidya, Comparative study on durability properties of engineered cementitious composites with polypropylene fiber and glass fiber, Arch. Civ. Eng. 63 (2017) 83–101, https://doi.org/10.1515/ace-2017-0042.
[17] H.J. Kong, S.G. Bike, V.C. Li, Constitutive rheological control to develop a self-consolidating engineered cementitious composite reinforced with hydrophilic poly(vinyl alcohol) fibers, Cem. Concr. Compos. 25 (2003) 333–341, https://doi.org/10.1016/S0958-9465(02)00056-2.
[18] Z. Wu, C. Shi, K.H. Khayat, Investigation of mechanical properties and shrinkage of ultra-high performance concrete: influence of steel fiber content and shape, Compos. B Eng. 174 (2019), 107021, https://doi.org/10.1016/j.compositesb.2019.107021.
[19] H.R. Pakravan, M. Jamshidi, M. Latifi, The effect of hydrophilic (polyvinyl alcohol) fiber content on the flexural behavior of engineered cementitious composites (ECC), J. Text. Inst. 5000 (2017), https://doi.org/10.1080/00405000.2017.1329132, 0.
[20] C.C. Ecc, Experimental Investigation of the Mechanical Properties of Engineered Experimental Investigation of the Mechanical Properties of Engineered Cementitious Composites, ECC), 2016.
[21] P. Zhang, Q.F. Li, J. Wang, Y. Shi, Y.F. Ling, Effect of PVA fiber on durability of cementitious composite containing nano-SiO2, Nanotechnol. Rev. 8 (2019) 116–127, https://doi.org/10.1515/ntrev-2019-0011.
[22] E.K. Anastasiou, I. Papayianni, M. Papachristoforou, Behavior of self compacting concrete containing ladle furnace slag and steel fiber reinforcement, Mater. Des. 59 (2014) 454–460, https://doi.org/10.1016/j.matdes.2014.03.030.
[23] P.Æ. Giovanni, P.Æ. Lucie, Fibre Reinforced Concrete : New Design Perspectives, 2009, pp. 1261–1281, https://doi.org/10.1617/s11527-009-9529-4.
[24] L.F. Maya Duque, B. Graybeal, Fiber orientation distribution and tensile mechanical response in UHPFRC, Mater. Struct. Constr. 50 (2017) 1–17, https://doi.org/10.1617/s11527-016-0914-5.
[25] L. Ferrara, Y.-D. Park, S.P. Shah, Correlation among fresh state behavior, fiber dispersion, and toughness properties of SFRCs, J. Mater. Civ. Eng. 20 (2008) 493–501, https://doi.org/10.1061/(asce)0899-1561(2008)20:7(493).
[26] P.K. Sridhara, F. Vilaseca, Assessment of fiber orientation on the mechanical properties of PA6/Cellulose composite, Appl. Sci. 10 (2020), https://doi.org/10.3390/app10165565.
[27] P. Stähli, R. Custer, J.G.M. Van Mier, On flow properties, fibre distribution, fibre orientation and flexural behaviour of FRC, Mater. Struct. Constr. 41 (2008) 189–196, https://doi.org/10.1617/s11527-007-9229-x.
[28] H.M. Niu, Y.M. Xing, Y. Zhao, Effects of processing on fiber distribution and mechanical performance of engineered cementitious composites(ECC), Adv. Mater. Res. 709 (2013) 122–126. https://doi.org/10.4028/www.scientific.net/AMR.709.122.
[29] S.H. Said, H. Abdul, The effect of synthetic polyethylene fi ber on the strain hardening behavior of engineered cementitious composite (ECC), JMADE 86 (2015) 447–457, https://doi.org/10.1016/j.matdes.2015.07.125.
[30] H. Reza, T. Ozbakkaloglu, Synthetic fibers for cementitious composites : a critical and in-depth review of recent advances, Construct. Build. Mater. 207 (2019) 491–518, https://doi.org/10.1016/j.conbuildmat.2019.02.078.
[31] H. Tran, J. Li, Y.X. Zhang, Numerical modelling of the flow of self-consolidating engineered cementitious composites using smoothed particle hydrodynamics, Construct. Build. Mater. 211 (2019) 109–119, https://doi.org/10.1016/j.conbuildmat.2019.03.210.
[32] L. Ferrara, N. Ozyurt, M. Di Prisco, High mechanical performance of fibre reinforced cementitious composites: the role of “casting-flow induced” fibre orientation, Mater. Struct. Constr. 44 (2011) 109–128, https://doi.org/10.1617/s11527-010-9613-9.
[33] M. Li, V.C. Li, Rheology , Fiber Dispersion , and Robust Properties of Engineered Cementitious Composites, 2013, pp. 405–420, https://doi.org/10.1617/s11527-012-9909-z.
[34] J. Zhou, S. Qian, G. Ye, O. Copuroglu, K. Van Breugel, V.C. Li, Improved fiber distribution and mechanical properties of engineered cementitious composites by adjusting the mixing sequence, Cem. Concr. Compos. 34 (2012) 342–348, https://doi.org/10.1016/j.cemconcomp.2011.11.019.
[35] T. Star, T. Committee, Strain Hardening Cement Composites : Structural Design and Performance, 2013.
[36] H. Huang, A. Su, X. Gao, Y. Yang, Influence of formwork wall effect on fiber orientation of UHPC with two casting methods, Construct. Build. Mater. 215 (2019) 310–320, https://doi.org/10.1016/j.conbuildmat.2019.04.200.
[37] V.C. Li, F.P. Bos, K. Yu, W. Mcgee, T. Yan, S. Chaves, K. Nefs, V. Mechtcherine, V. Naidu, J. Pan, G.P.A.G. Van Zijl, P.J. Kruger, On the emergence of 3D printable engineered , strain hardening cementitious composites (ECC/SHCC), Cement Concr. Res. 132 (2020), 106038, https://doi.org/10.1016/j.cemconres.2020.106038.
[38] B. Zhou, Y. Uchida, Influence of flowability, casting time and formwork geometry on fiber orientation and mechanical properties of UHPFRC, Cement Concr. Res. 95 (2017) 164–177, https://doi.org/10.1016/j.cemconres.2017.02.017.
[39] J. Martin, Understanding and overcoming shear alignment of fibers during extrusion, Soft Matter 11 (2014) 400–405, https://doi.org/10.1039/C4SM02108H.
[40] P. Groth, D. Nemegeer, The Use of Steel Fibres in Self-Compacting Concrete, First Int. RILEM Symp. Self-Compacting Concr, 1999, pp. 497–507.
[41] H. Huang, X. Gao, L. Li, H. Wang, Improvement effect of steel fiber orientation control on mechanical performance of UHPC, Construct. Build. Mater. 188 (2018), https://doi.org/10.1016/j.conbuildmat.2018.08.146.
[42] Z. Ge, A.M. Tawfek, H. Zhang, Y. Yang, H. Yuan, R. Sun, Z. Wang, Influence of an extrusion approach on the fiber orientation and mechanical properties of engineering cementitious composite, Construct. Build. Mater. 306 (2021), 124876, https://doi.org/10.1016/j.conbuildmat.2021.124876.
[43] H. Zhang, L. Zhu, F. Zhang, M. Yang, Effect of Fiber Content and Alignment on the Mechanical Properties of 3D Printing Cementitious Composites, 2021, pp. 1–17.
[44] D.Y. Yoo, G. Zi, S.T. Kang, Y.S. Yoon, Biaxial flexural behavior of ultra-high-performance fiber-reinforced concrete with different fiber lengths and placement methods, Cem. Concr. Compos. 63 (2015) 51–66, https://doi.org/10.1016/j.cemconcomp.2015.07.011.
[45] Interface Property and Apparent Strength of High-Strength Hydropidlic Fiber in Cement Matrix, 1998, pp. 5–13.
[46] K. Wille, N.V. Tue, G.J. Parra-Montesinos, Fiber distribution and orientation in UHP-FRC beams and their effect on backward analysis, Mater. Struct. Constr. 47 (2014) 1825–1838, https://doi.org/10.1617/s11527-013-0153-y.
[47] J. Bi, Y. Zhao, J. Guan, L. Huo, H. Qiao, L. Yuan, Three-dimensional modeling of the distribution and orientation of steel fibers during the flow of self-compacting concrete, Struct. Concr. 20 (2019) 1722–1733, https://doi.org/10.1002/suco.201900072.
[48] T. Oesch, E. Landis, D. Kuchma, A methodology for quantifying the impact of casting procedure on anisotropy in fiber-reinforced concrete using X-ray CT, Mater. Struct. Constr. 51 (2018) 1–13, https://doi.org/10.1617/s11527-018-1198-8.
[49] M. Miletić, L. Mohana, J. Arns, A. Agarwal, S.J. Foster, C. Arns, D. Perić, Cement and Concrete Research Gradient-based fibre detection method on 3D micro-CT tomographic image for defining fibre orientation bias in ultra-high-performance concrete, Cement Concr. Res. 129 (2020), 105962, https://doi.org/10.1016/j.cemconres.2019.105962.
[50] F. Laranjeira, A. Aguado, C. Molins, S. Grünewald, J. Walraven, S. Cavalaro, Framework to predict the orientation of fibers in FRC: a novel philosophy, Cem, Concr. Res. 42 (2012) 752–768, https://doi.org/10.1016/j.cemconres.2012.02.013.
[51] L. Tutluoğlu, İ.F. Öge, C. Karpuz, Relationship between pre-failure and post-failure mechanical properties of rock material of different origin, Rock Mech. Rock Eng. 48 (2015) 121–141, https://doi.org/10.1007/s00603-014-0549-1.
[52] M. Gesoğlu, E. Güneyisi, G.F. Muhyaddin, D.S. Asaad, M.E. Yılmaz, Strain hardening ultra-high performance fiber reinforced cementitious composites: effect of fiber type and concentration, Composer Part B. (2016), https://doi.org/10.1016/j.compositesb.2016.08.004.
[53] H.H. Qadir, R.H. Faraj, A.F.H. Sherwani, B.H. Mohammed, K.H. Younis, Mechanical properties and fracture parameters of ultra high performance steel fiber reinforced concrete composites made with extremely low water per binder ratios, SN Appl. Sci. 2 (2020), https://doi.org/10.1007/s42452-020-03425-3.

[54] H. Nakamura, T. Nanri, T. Miura, S. Roy, Experimental investigation of compressive strength and compressive fracture energy of longitudinally cracked concrete, Cem. Concr. Compos. 93 (2018) 1–18, https://doi.org/10.1016/j.cemconcomp.2018.06.015.
[55] S.M.J. Razavi, L. Sandnes, J. Torgersen, F. Berto, The effect of fiber orientation on fracture response of metallic fiber-reinforced adhesive thin films, Theor. Appl. Mech. Lett. 8 (2018) 43–47, https://doi.org/10.1016/j.taml.2018.01.001.
[56] G. Van Zijl, M.J. Tan, Properties of 3D Printable Concrete, 2017.
[57] P. Sadeghian, A.R. Rahai, M.R. Ehsani, Effect of fiber orientation on compressive behavior of CFRP-confined concrete columns, J. Reinforc. Plast. Compos. 29 (2010) 1335–1346, https://doi.org/10.1177/0731684409102985.
[58] T. Vincent, T. Ozbakkaloglu, Influence of fiber orientation and specimen end condition on axial compressive behavior of FRP-confined concrete, Construct. Build. Mater. 47 (2013) 814–826, https://doi.org/10.1016/j.conbuildmat.2013.05.085.
[59] C.T. Sun, A.W. Jun, Compressive strength of unidirectional fiber, Compsite Sci. Technol. 52 (1995) 577–587.
[60] K.G. Satish, B. Siddeswarappa, K.M. Kaleemulla, Characterization of in-plane mechanical properties of laminated hybrid composites, J. Miner. Mater. Char. Eng. 9 (2010) 105–114, https://doi.org/10.4236/jmmce.2010.92009.
[61] P. Riedel, T. Leutbecher, Einfluss der Faserorientierung und des Fasergehalts auf die Druckfestigkeit von ultrahochfestem Beton, vol. 115, 2020, pp. 1–12, https://doi.org/10.1002/best.202000020.
[62] H.H. Qadir, R.H. Faraj, A.F.H. Sherwani, B.H. Mohammed, K.H. Younis, Mechanical properties and fracture parameters of ultra high performance steel fiber reinforced concrete composites made with extremely low water per binder ratios, SN Appl. Sci. 2 (2020) 1–12, https://doi.org/10.1007/s42452-020-03425-3.
[63] I. Curosu, E. Muja, M. Ismailov, A.H. Ahmed, M. Liebscher, V. Mechtcherine, An experimental-analytical scale-linking study on the crack-bridging mechanisms in different types of SHCC in dependence on fiber orientation, Cement Concr. Res. 152 (2022), 106650, https://doi.org/10.1016/j.cemconres.2021.106650.
[64] L. Teng, H. Huang, J. Du, K.H. Khayat, Prediction of fiber orientation and flexural performance of UHPC based on suspending mortar rheology and casting method, Cem. Concr. Compos. 122 (2021), 104142, https://doi.org/10.1016/j.cemconcomp.2021.104142.
[65] Q. Chen, J. Lang, J. Wang, Flexural properties of bamboo-log composite beam, J. Eng. Sci. Technol. Rev. 11 (2018) 104–112, https://doi.org/10.25103/jestr.113.14.
[66] M.S. Choi, S.T. Kang, B.Y. Lee, K.T. Koh, G.S. Ryu, Improvement in predicting the post-cracking tensile behavior of ultra-high performance cementitious composites based on fiber orientation distribution, Materials 9 (2016), https://doi.org/10.3390/ma9100829.
[67] D.Y. Yoo, S.T. Kang, J.H. Lee, Y.S. Yoon, Effect of shrinkage reducing admixture on tensile and flexural behaviors of UHPFRC considering fiber distribution characteristics, Cement Concr. Res. 54 (2013) 180–190, https://doi.org/10.1016/j.cemconres.2013.09.006.
[68] B.V.C. Li, C.K.Y. Leung, Steady-state and multiple cracking of short random fiber composites, J. Eng. Mech. 118 (1993) 2246–2264.
[69] C. Materials, Improved Sectional Image Analysis Technique for Evaluating Fiber Orientations in Fiber-Reinforced, 2016, pp. 1–13, https://doi.org/10.3390/ma9010042.
[70] M. Qiu, Y. Zhang, S. Qu, Y. Zhu, X. Shao, Effect of reinforcement ratio, fiber orientation, and fiber chemical treatment on the direct tension behavior of rebar-reinforced UHPC, Construct. Build. Mater. 256 (2020), 119311, https://doi.org/10.1016/j.conbuildmat.2020.119311.
[71] S. Kim, H. Yun, Composites : Part B Crack-damage mitigation and flexural behavior of flexure-dominant reinforced concrete beams repaired with strain-hardening cement-based composite, Composer Part B. 42 (2011) 645–656, https://doi.org/10.1016/j.compositesb.2011.02.022.
[72] Y. Wang, F. Liu, J. Yu, F. Dong, J. Ye, Effect of polyethylene fiber content on physical and mechanical properties of engineered cementitious composites, Construct. Build. Mater. 251 (2020), 118917, https://doi.org/10.1016/j.conbuildmat.2020.118917.
[73] B.T. Huang, K.F. Weng, J.X. Zhu, Y. Xiang, J.G. Dai, V.C. Li, Engineered/strain-hardening cementitious composites (ECC/SHCC) with an ultra-high compressive strength over 210 MPa, Compos. Commun. 26 (2021), 100775, https://doi.org/10.1016/j.coco.2021.100775.
[74] B. Shan, S. Zheng, J. Ou, A Stereovision-based Crack Width Detection Approach for Concrete Surface Assessment, KSCE J. Civ. Eng. (2015) 1–10, https://doi.org/10.1007/s12205-015-0461-6, 00.
[75] S. Backers, A micromechanical model of tension-softening and bridging toughening of short random fiber reinforced brittle, J. Mech. Phys. Solid. 39 (1991) 607–625.
[76] J. Zhang, V.C. Li, Effect of inclination angle on fiber rupture load in fiber reinforced cementitious composites, Compos. Sci. Technol. 62 (2002) 775–781, https://doi.org/10.1016/S0266-3538(02)00045-3.
[77] V. Li, Tensile Strain-Hardening Behavior or Polyvinyl Alcohol Engineered Cementitious Composite, PVA-ECC), 2001.